11TH INTERNATIONAL SYMPOSIUM ON PARTICLE IMAGE VELOCIMETRY - PIV15
Santa Barbara, California, September 14-16, 2015

Simultaneous velocity and concentration field measurements of pulsating and heated coaxial turbulent jets in square turbulent duct flow

J. Klinner[1], C. Willert[1], W. Förster[1], M. Beversdorff[1] and V. Mayer[2]

[1] Institute of Propulsion Technology, German Aerospace Center (DLR), 51170 Köln, Germany
chris.willert@dlr.de

[2] Daimler AG, D-70546 Stuttgart, Germany

ABSTRACT

Simultaneous velocity and concentration measurements of the mixing of a confined coaxial jet in air are performed in a small scale windtunnel at atmospheric pressure, constant mass flow rates and three modes of operation: isothermal steady jet injection (Re_d = 32000); pulsed isothermal injection (St=0.08) and steady injection at elevated jet temperatures of ΔT=50 K and ΔT=100 K. Instantaneous measurements of mass fraction are implemented using planar laser induced fluorescence (PLIF) of the acetone seeded injected flow. Simultaneous two-component velocity measurements are performed using particle image velocimetry (PIV). The contribution provides details of the PLIF-PIV measurement setup, data evaluation and accuracy estimation. Stochastic error convergence over the number of samples is assessed within the turbulent shear layer for first and second moments of velocity and mass fraction. Results from all modes of operation are discussed on the basis of velocity, mass fraction, Reynolds shear stress and turbulent mass flux.

1. Introduction

The present investigation is motivated by the performance assessment of established numerical methods with regard to prediction of turbulent scalar transport and mixing. In particular the optimization of exhaust gas recirculation and urea injection for NOx-reduction in internal combustion engines requires a detailed knowledge of mixing processes of the engines' gas, oxygen, fuel and additives. The optimization of the reactor and mixing port geometry by computational fluid dynamics (CFD) requires experimental data to validate the underlying Reynolds stress and mass transport models.

To address this demand a generic mixing experiment is designed to provide relevant data of turbulence induced mass transfer to validate scalar transport simulations. The measurements are performed in a small scale wind tunnel as outlined in Fig. 1. The mixing port is placed at a third of the test section length and consists of a 90° bend. The bend exit is aligned coaxially to the channel's center line. Three modes of operation are investigated at constant mass flow rates: (A) isothermal steady jet injection (c.f. [4]), (B) pulsed isothermal injection with a pulsation frequency of 66 Hz and a Strouhal number of 0.08 and (C) steady injection at elevated jet temperatures of ΔT=50 K and ΔT=100 K.

The measurements are aimed at providing statistically converged quantities of velocity and concentration, turbulent fluctuations and the degree of correlation of these fluctuations. Ensemble-averages of velocity, mass fraction, Reynolds stresses and turbulent mass flux are

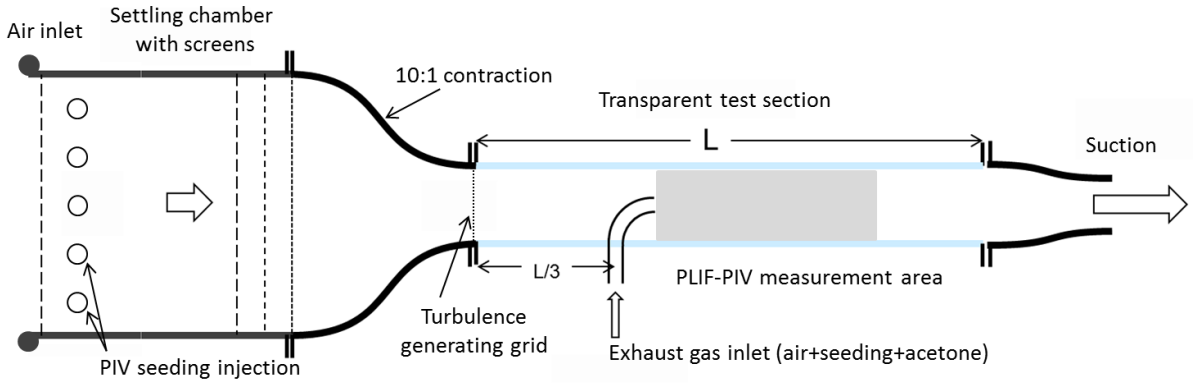

Figure 1: Schematic diagram of wind tunnel facility with approximate location of acetone PLIF and PIV measurement area

determined at specific positions downstream of the nozzle using sets of up to 3600 PLIF-PIV recordings. During pulsed operation, phase angles are simultaneously monitored with each single shot to enable a posteriori phase sorting and phase averaging. Unlike a phase locked measurement, phase sorting allows averaging at arbitrary cycle positions using arbitrary bin sizes and provides insight into the flow evolvement during an entire pulsation cycle without a priori knowledge of explicit cycle positions.

The measurement uncertainty of each velocity component is estimated from uncertainties of the displacement detection. The stability of the initial acetone tracer concentration over time is assessed from fluorescence measurements of unmixed fluid. The systematical error due to temperature dependency of fluorescence quantum yield is discussed and partially corrected. The statistical error of measured quantities over the number of samples is assessed in exemplary regions within the shear layers of the mixing zone during steady injection.

2. Test Facility and Operation Conditions

The wind tunnel (see Fig. 2) is operated in suction mode and has a 830 mm long test section with a square cross-section of internal width of 76 mm. Quartz windows with 45° edge bevels provide optical access to the entire cross-section. Flow conditioning is provided by a settling chamber containing screens and straightening tubes. Reproducible turbulent flow conditions are provided by a turbulence grid made of perforated steel that is placed immediately upstream of the test section at the exit of contraction nozzle. The turbulent fluctuations of the main flow immediately upstream of the mixing port have decayed to levels of $Tu = 0.02$ which is verified by planar PIV measurements at center plane. Relevant operation parameters of the tunnel are provided in Table 1. Under steady isothermal operation the Reynolds number of the incoming main flow of the tunnel is 16000 and the Reynolds number of the injected air is 32000, both of which are based on bulk velocities and hydraulic diameter. Under steady isothermal operation the Reynolds number is 26000 based on the differences of bulk velocities of both streams and on the diameter of the injection port. During steady isothermal operation the exhaust gas flow is injected into the tunnel flow at approximately half of the inlet mass flow rate. The friction velocities u_τ at both inlets given in Table 1 are obtained from near-wall PIV measurements as reported in [9]. The friction velocity at tunnel outlet is based on the model of a flat plate and the pressure difference from pressure tabs at tunnel inlet and outlet.

The wind tunnel is mounted on an $x-y$ translation stage to enable measurements in different regions while the PLIF-PIV setup remains stationary. The measurement results within this contribution are obtained at the channel $x-z$ and $x-y$ center planes and are measured in the mixing zone between $x = 0-300\,mm$ equivalent to 0-12 nozzle diameters.

	Symbol	Tunnel inlet	Injection inlet	Tunnel Outlet	Units
Position	x	-110	0	200	mm
Mass flow	$\dot{m}$	22.5	11.5	34	g/s
Hydraulic diameter	D (tunnel), d (nozzle)	76	25	76	mm
Bulk velocity	u_0	3.25	19.5	4.9	m/s
Reynolds number based on d,D and u_0	Re	16250	32000	24500	
Friction velocity at upper wall	u_τ	0.199	0.181	0.265	m/s

Table 1: Flow paramter during steady isothermal injection

3. Combined Acetone PLIF/PIV Setup

The optical setup for the combined PLIF-PIV measurements is depicted in Fig. 2. Instantaneous concentration measurements are implemented

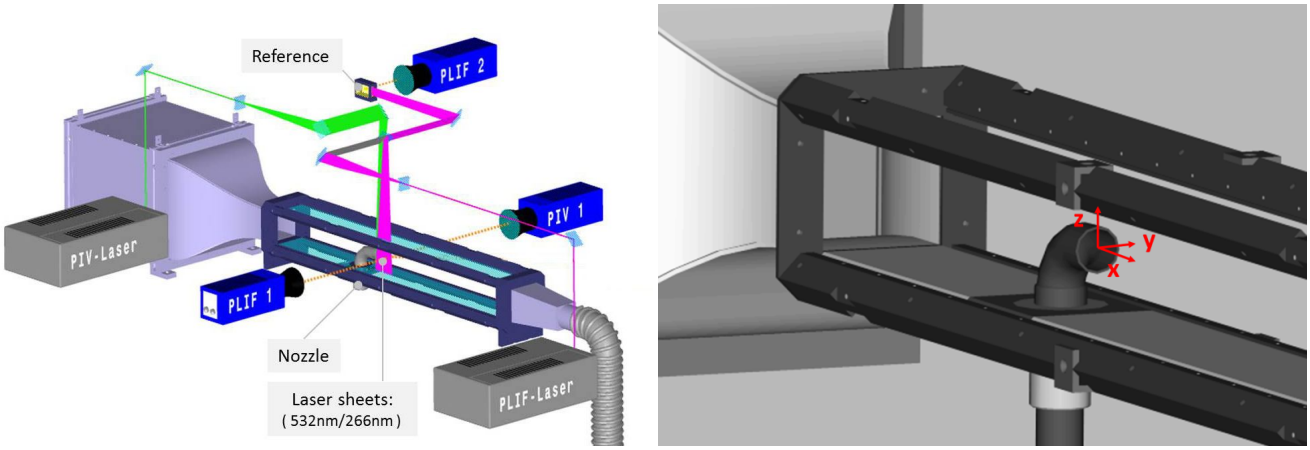

Figure 2: Schematic of the combined PLIF-PIV experimental setup (left) for measurements in the x-z plane of the nozzle coordinate system (right)

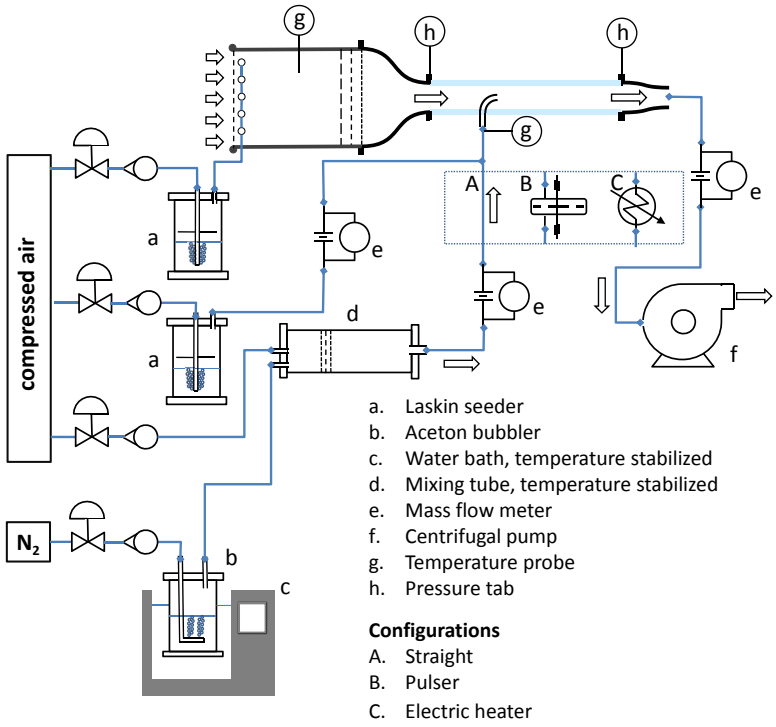

Figure 3: Flow chart and instrumentation of the wind tunnel

using planar laser induced fluorescence (PLIF) of the acetone seeded injected flow following the work of [2], [5], [7]. The Acetone is excited with a quadrupled Nd:YAG pulse laser at 266 nm resulting in fluorescence in a spectral range of 320...600 nm [2]. Images of the acetone fluorescence are acquired with an intensified camera (Dicam-Pro, PCO AG) equipped with a S20Q photocathode and a Nikkor 50/$f_{\#}$1.2 lens. Pixel binning by a factor of 2×2 increases the signal yield but does not compromise the spatial resolution which is limited by micro-channel plate. After binning the spatial resolution is 6 pixel/mm.

The pulsed UV-laser has a pulse energy of 80 mJ at 266 nm and a pulse width of 12 ns (Quanta Ray, Spectra Physics). The laser beam is converted into a divergent light sheet of 80μm thickness which has a width of 120 mm at the center of the wind tunnel. A short pass edge filter with a 65% cut off wavelength at 500 nm is placed in front of the lens to protect the camera's intensifier from the 532 nm light scattered by the PIV laser light. The camera's photocathode is gated at 40 ns coinciding with the UV-laser pulse. The intensifier's gain is set to 20-30%.

Using a beam splitter plate, roughly 4% of the PLIF laser sheet energy is guided to a reference cell filled with a rhodamine 6G ethanol mixture. Permanent recycling of the fluid using a circulation pump and a reservoir prevents degradation of the dye due to bleaching. The green fluorescence of the dye is imaged by another CCD camera (PCO.1600, PCO AG). Acquired simultaneously with every acetone fluorescence image, the dye fluorescence images are subsequently used to determine the instantaneous excitation intensity profile thereby enabling shot-to-shot intensity normalization [4] and [3].

In parallel to the PLIF measurements simultaneous planar 2-C velocity measurements are obtained using particle image velocimetry (PIV) in a conventional orthogonal viewing arrangement. The dual frame sCMOS camera (ILA.sCMOS.PIV, ILA GmbH) is equipped with a 85mm lens (Zeiss Planar T1.4/85 ZF.2) with an aperture of $f_{\#}$5.6 and observes the field of view at a magnification of approximately 22 pixel/mm. Paraffin tracer droplets injected upstream of the wind tunnel's flow straighteners are illuminated using a frequency doubled Nd:YAG laser with a rated pulse energy of 50 mJ at 532 nm (Brilliant Twins, Quantel/BigSky Laser). For the experiments at elevated jet temperatures the injection port is seeded using a Laskin atomizer filled with a highly refined hydrocarbon mineral oil (Vicount Smoke Oil 135/180) which has a higher boiling temperature than paraffine oil which tended to evaporate prior to injection into the co-flow. In comparison the scattering diameter of the (partially evaporated) oil droplets at the mixing port outlet at T=393K (ΔT=100 K) is still large enough to provide sufficiently high intensity for PIV. Bandpass filters with a spectral width of 10 nm and a center wavelength of 532 nm reject stray light. Both, the inlet flow and the injected flow are seeded at matching tracer concentrations. Under isothermal conditions the seeding consists of paraffin aerosol created by two Laskin atomizers. Impactors in the seeding device reduce the size fraction below 1 μm prior to introducing the seeded air respectively to the settling chamber and mixing tube.

Trigger pulses for all lasers and cameras are generated by a programmable timing generator (PIVseqPCI, PIVTEC GmbH). The acquisition rate of the combined measurements is 5 Hz which is a compromise of having all lasers operating at optimum flash lamp repetition rates (10 and 15 Hz) while all Q-switches are triggered at a common frequency. The pulse separation for PIV Δt was set in a range of

25...35 μs according to displacement PDFs to have an ideal particle image displacement of 10 pixel and validation rates of at least 85% in the shear layers. The timing of a single PLIF-PIV measurement was chosen in such a way that the PLIF laser pulse is placed exactly in between the PIV laser pulses at $\Delta t/2$. At pulsating injection, the phase angle of each combined PLIF-PIV single shot is recorded using two counter channels of a digital data acquisition card (ADWIN-16) running at sampling rate of 20 kHz.

The flow chart in Fig. 3 shows the instrumentation of the wind tunnel air supply and suction system as well as the PIV seeding and acetone supply. Orifice plates and a laminar flow meter are used to monitor the suction and injection mass flow rates. During long PLIF-PIV acquisition runs (12 minutes, 3600 images at 5Hz frame rate) the suction mass flow is stable to within $\pm 0.4\%$ and the injected mass flow is stable to within $\pm 0.2\%$ with respect to the mean mass flow rates. About 0.5 vol% tracer gas concentration are added to the injected flow. The acetone bubbler, the mixing tube and the acetone supply lines upstream of the mixing tube are temperature stabilized to avoid acetone condensation and to keep the acetone tracer concentration stable during the long runs.

4. Data Evaluation and Accuracy Estimation

4.1 PIV Image Processing

The PIV image data is processed using PIVview 3.6.0 (PIVTEC GmbH) for which the PIV evaluation parameters are summarized in Table 2. Particle displacements are recovered using a coarse-to-fine multi-grid processing scheme with image deformation at each step to take into account the strong shear in the flow. The sub-pixel correlation peak position measurement was performed by a truncated sinc signal reconstruction algorithm. Due to this processing and a sufficiently high particle image density an accuracy of correlation peak detection below 0.1 pixel can be obtained for regions without strong laser background and without strong velocity gradients. Given the magnification of 22 pixel/mm and a pulse delay of $\Delta t = 25 - 35\,\mu$s, a peak detection accuracy of 0.1 pixel would lead to a absolute velocity uncertainty of $0.13 - 0.18$ m/s.

Field of view	116×80 (overview) 19×80 (statistics)	mm
	2560×1760 (overview) 420×1760 (statistics)	pixel
Magnification	22.0	pixel/mm
Pulse delay	25 - 35	μs
Window size	2.18×1.45	mm
	48×32	pixel
Sampling	1.09×0.73	mm
	24×16	pixel
Interrogation method	Multi-grid + Image deformation	
Peak detection	Whittaker reconstruction	
Vector validation test	max. displacement diff. (10 pixel),normalized median (6)	

Table 2: PIV evaluation parameters

4.2 PLIF Image Processing

After background subtraction, PLIF images are first flat-field corrected. For this purpose, images are divided by a sensitivity image, which is recorded while the channel is flooded with a homogeneous acetone tracer concentration (average over 200 images). This procedure accounts for the angular lens collection efficiency, variations of sensitivity of the camera, the quantum efficiency of fluorescence and, most importantly, spatial variations of laser intensity. In order to correct for additional shot-to-shot fluctuations of the local excitation energy, each single image at t_i is corrected according to using the unsteady intensity distribution determined from the rhodamine cell recordings. A detailed description of image processing procedure can be found in [4]).

Prior to the calculation of the turbulent mass flux $\langle u_i' c' \rangle$ the photon/pixel noise in the PLIF images is removed to some extent by a Gaussian low pass filter. The kernel size of the low pass filter is set to a fraction of 1⁄4 of the PIV interrogation window size. Thus, after filtering, the spatial resolution of PLIF concentration fields is still above the spatial resolution of velocity measurements.

Both accurate absolute or relative concentration measurements require a temporally stable and homogeneous initial acetone tracer density at the injection port. Fig. 4 shows the stability of the PLIF signal at maximum (unmixed) acetone concentration within a rectangular region immediately downstream of the injection inlet during a run of 12 minutes with 5 Hz acquisition rate. The acetone fluorescence signal slightly fluctuates within the first 800 measurements and remains stable throughout the remainder of the sequence with a 4.8% standard deviation from the average. The same signal S_{f0} is then used to scale PLIF images to maximum concentration to obtain the respective mass fraction. The reference is directly obtained from single-shot images if the injection inlet is within the field of view. If the injection inlet is outside the field of view the maximum concentration is acquired prior and after each measurement and then linearly interpolated. Thus, long-time deviations of the initial acetone concentration are compensated to first order.

As described by Thurber et al. [7], the fluorescence of acetone exhibits a temperature dependency which will bias mass fraction measurements especially at elevated temperatures. Following the temperature calibrations for atmospheric pressure reported by Thurber et al. [7] the acetone fluorescence roughly decreases by $3 - 4\%$ between 330 and 395 K at an excitation wavelength of 266 nm. The calibration curve

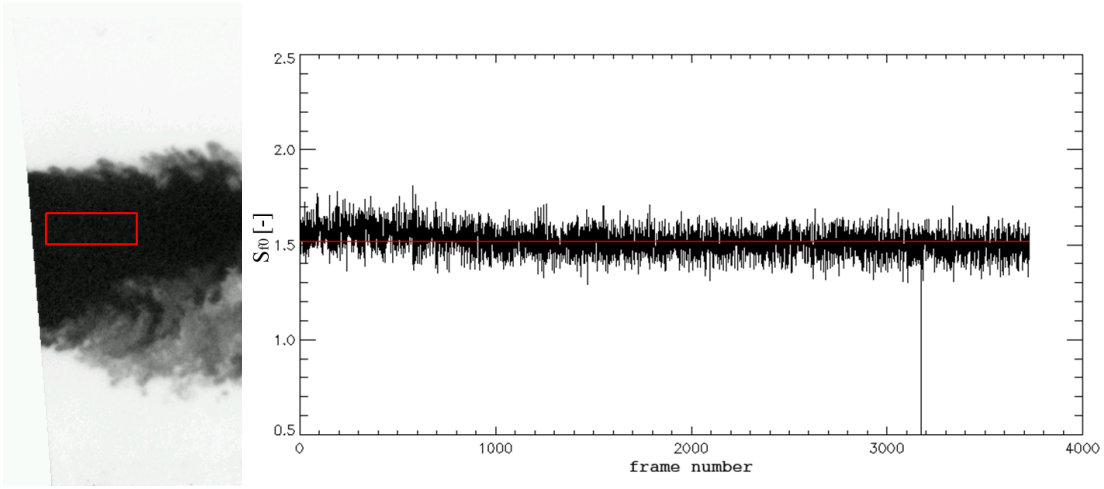

Figure 4: Stability of the unmixed fluorescence signal immediately downstream of the nozzle in the highlighted rectangular region. 3600 frames correspond to an acquisition time of 12 min

from Thurber et al. allows a first order correction of the temperature dependency of mass fraction at each image position

$$c_1 = \frac{S_{f1}}{S_{f0}} \frac{Qy(T_0)}{Qy(T_1)}, \tag{1}$$

where S_{f1} is the measured fluorescence at each pixel, S_{f0} is the unmixed acetone fluorescence immediately upstream of the nozzle exit, $Qy(T)$ is the quantum yield of the temperature dependent fluorescence per molecule per unit laser fluence at T_0 respectively T_1. Mixing temperatures for quantum yield corrections are estimated from local mass fraction.

4.3 Sampling Error Estimation

The uncertainty of time-averaged velocity, mass fraction, Reynolds shear stress and turbulent mass flux over the number of samples is assessed by empirical bootstrapping, similar to an approach published by Stafford et al. [6]. Bootstrapping relies on random sampling with replacement and can be used to estimate the random error (e.g. confidence interval) of quantities with unknown distributions [1].

Each bootstrap $X_b^* = \{x_1, x_2, ..., x_N\}$ is a subset of N samples comprising the entire data set. Each sample is selected using a random generator. The statistical error of each measured quantity x is estimated on the basis of the relative deviation from a reference value

$$E_r(\overline{X}_b^*) = \frac{\overline{X}_b^* - \overline{X}_B}{\overline{X}_B}, \tag{2}$$

where $\overline{X}_B$ is the bootstrap which contains the entire data set. The accuracy of PIV velocity components in x, y and z direction (u, v, w) are not independent due to a unique pulse separation Δt which is set according to the maximum displacement without loss of pairs. Thus, $\overline{u}_B$ is used in the denominator of Eq. (2) as reference for the stochastic error estimation of u, v, w.

5. Results

5.1 Random Error Assessment

The convergence of the previously defined error estimator versus number of samples is evaluated for regions in the turbulent shear layer during isothermal and steady injection. Data from upstream regions A,B,C with the size matching a single PIV interrogation window are evaluated. Positions of these three regions are highlighted in the RMS plots shown in Fig. 5. These regions were chosen because they are most susceptible to PIV signal loss due to the presence of high shear stress. A pronounced turbulent mass flux is expected in these regions due to presence of fluctuations of both velocity and concentration.

Fig. 6 shows the decreasing random error of $\langle u \rangle$ and $\langle u'u' \rangle$ against the 3000 sample statistics in region A. Each distribution contains 500 bootstraps. Estimates of statistical error based on the size of the 95% confidence interval of normally distributed data ($\pm 2\sigma$). The error of $\langle u \rangle$ is below 1% from 1500 samples. Second order moments require significantly more samples to converge. From 2000 samples the error of $\langle u'u' \rangle$ against the 3000 sample statistics is in the order of 4%.

In Fig. 7, the convergence of the 95% confidence interval towards the 3000 sample statistics of all measured quantities in regions A,B and C is presented. Each confidence interval relies on PDFs of 1000 bootstraps. The error found by bootstrapping is fitted against the standard error of normally distributed data using the function $E_r = a/\sqrt{N}$. For first order statistics of normally distributed data the fit parameter can

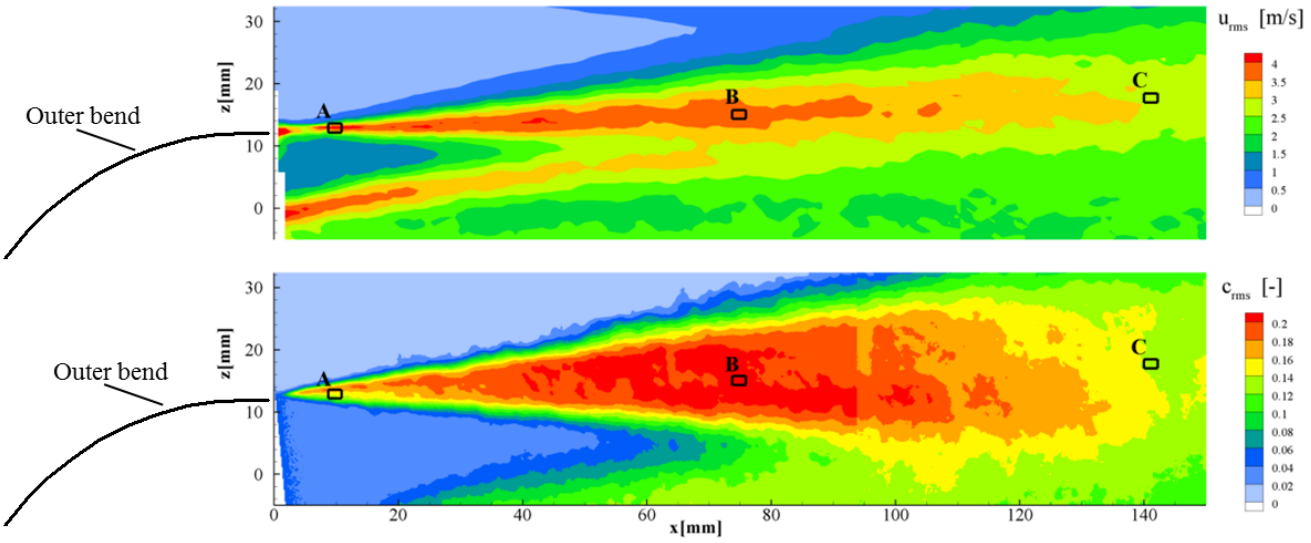

Figure 5: RMS of 500 samples with regions within which convergence tests are conducted

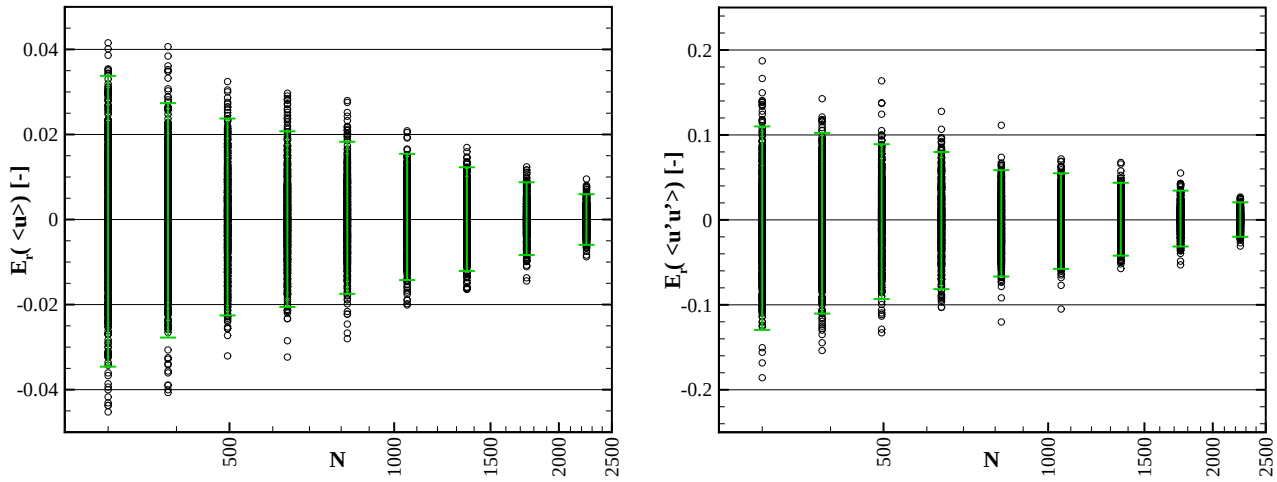

Figure 6: Random error in velocity (left) and Reynolds shear stress (right) over a 3000 sample data set in region A (Fig. 5); the error bar represents the 95% confidence interval

be expressed as $a = \sigma$ and for second order statistics $a = \sqrt{2}\sigma^2$ applies. Both, empirical and theoretical error are in good agreement for $N < 1000$. As the sample size increases, the error found by bootstrapping strongly converges towards zero with respect to the reference statistics (3000 samples). Therefore, above 1000 samples the relative error is estimated by extrapolation of the standard error fit. From 3000 samples the statistical error of $\langle u \rangle$, $\langle w \rangle$ and $\langle c \rangle$ is below 1% in all regions while the error of $\langle u'u' \rangle$ and $\langle v'v' \rangle$ is below 5%. Components of the turbulent mass flux $\langle u'w' \rangle$ and $\langle u'c' \rangle$ have an error below 6% from 3000 samples.

5.2 Concentration Field During Steady Isothermal Injection

The single shot of mass fraction and velocity presented in Fig. 8 provides an impression of the turbulent character of the flow. Large vortices in the upper shear layer indicates large scale mixing. These vortices break up into small-scale velocity fluctuations which accelerate the mixing and diffusion. Faster mixing and diffusion occurs in the lower area of the jet possibly due to the radial pressure gradient at the 90° bend exit causing ambient air to be sucked in. Another reason might be the wake of the bent which induces significant out-of-plane motion. The ensemble average over 500 single shots in Fig. 9 confirms a stronger mixing and diffusion in the wake of the 90° bend. Faster mixing occurs in $x-z$ center plane in comparison to the $x-y$ center plane. The jet potential core is deformed towards the outer radius of the bend with the higher momentum fluid remaining unmixed the longest. Mass fraction and velocity fields during steady isothermal injection are compared to RANS scalar transport simulations in [4].

5.3 Pulsed Isothermal Injection

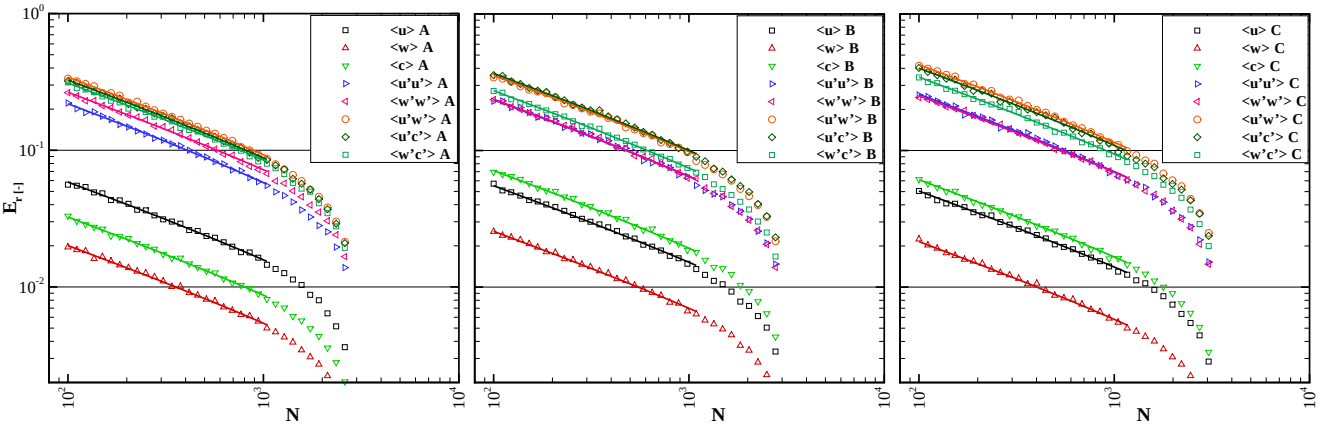

Figure 7: Relative error indicating 95% confidence in velocity, mass fraction, Reynolds shear stress and turbulent mass flux in regions A (left) B (middle) and C (right) in convergence towards the 3000 sample statistics

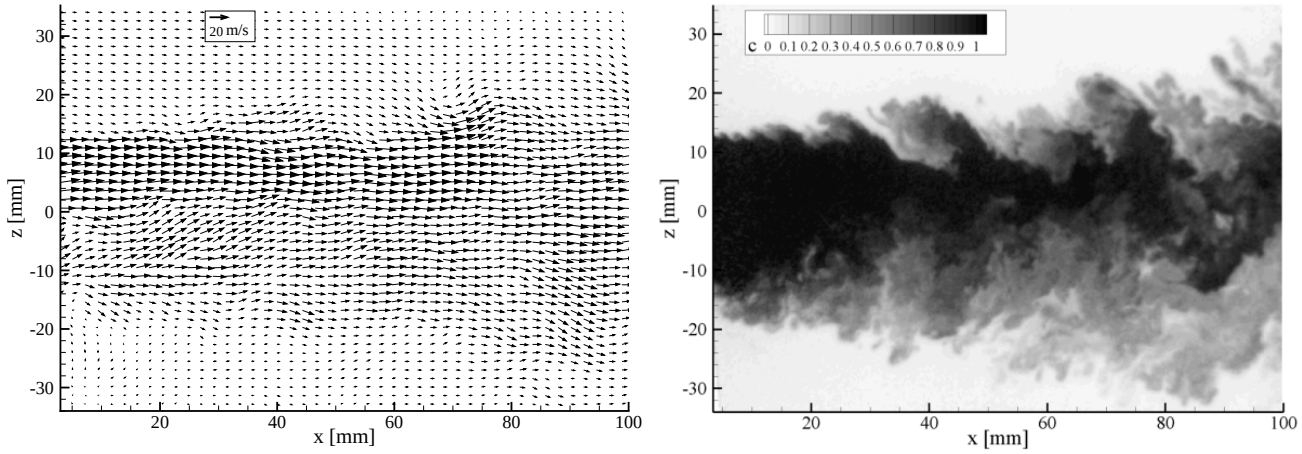

Figure 8: Snapshot of simultaneous velocity (2x2 vector skip) and concentration fields in the $x-z$ center plane with isothermal steady injection

Fig. 10 shows single shots of the mass fraction during pulsed operation in the $x-z$ center plane: (1) beginning of the injection phase,(2) strong injection and asymmetric vortex growing on the edges,(3) flow breakdown leaving behind small vortices and (4) again strong injection and forming of a large asymmetric vortex ring. Averaging of the entire PLIF sequence of all 3700 shots reveals that the concentration field within the $x-z$ center plane becomes even more asymmetric during pulsed injection in comparison to steady injection. Fig. 11 presents the time-averaged mass fraction at three upstream positions. The initial average concentration near the injection port (Fig. 11, left) is lower in comparison to the steady injection due to temporal flow breakdowns. Stronger mixing and diffusion occurs within the outer shear layer. Thus, the concentration field is skewed toward the upper channel side as shown in Fig. 11, middle and right.

Phase averaging of single shot PLIF-PIV measurements in the $x-z$ center plane gives a better insight into the temporal shear layer and vortex evolvement during a pulsation cycle. Phase sorting of the single shot measurements is performed on the data using 36 equidistant bins (10° bin size). The bin size is a compromise of having a sufficiently large sample count per bin (100 samples on average) while keeping the spatial smoothing due vortex motion to a minimum. According to convergence tests (c.f. Sect.) the random uncertainty of mean velocity and concentration on the basis of 100 samples would be in the order of $5-6\%$. At this state of work the stability of operation conditions would not allow to significantly extend the sample size. Fig. 12 shows phase averaged velocity and concentration fields at the beginning of injection (top) and during flow breakdown (bottom). Vortex centers and strength are detected using the λ_2 discriminant of non-linear eigenvalues of the velocity gradient tensor as described in [8]. At ($\Phi = 320°$) small vortices appear immediately upstream of the nozzle exit. At ($\Phi = 340°$) the outer vortex has moved almost twice the distance with respect to the inner vortex which leads to a faster vortex and higher growth due to entrainment. This effect seems to support stronger mixing and diffusion in the outer shear layer in comparison to the inner shear layer as confirmed in Fig. 11 (middle and right sub-figures). During flow breakdown velocities of the (inner) shear layer are not only reduced but also exhibit directional changes (forward at $\Phi = 160°$, upward at $\Phi = 200°$) including partial flow reversal ($\Phi = 240°$). Flow stagnation and reversal is accompanied by a wave-like variation of the concentration field at $\Phi = 240°$.

5.4 Elevated Jet Temperature

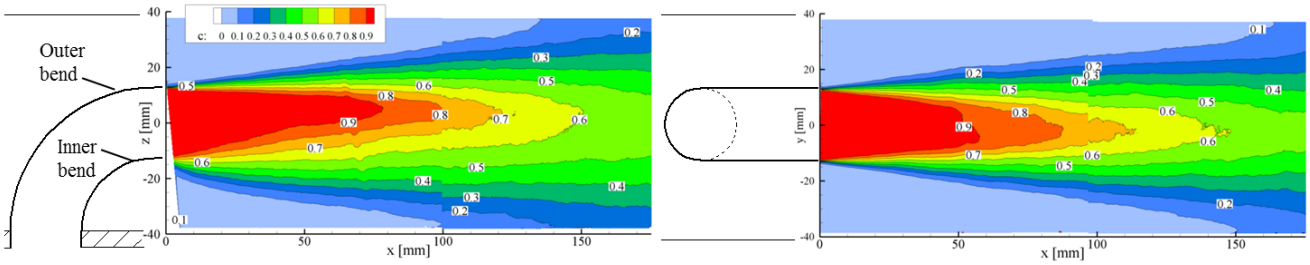

Figure 9: Isothermal concentration field with steady injection (Average over 500 samples)

The increased jet temperature leads to higher velocities within the jet due to decreasing air density at the given mass flow rate. This is confirmed by PIV measurements of the axial velocity in the $x-y$ center plane are presented in Fig. 13.

In Fig. 14, mass fraction profiles at three different jet temperatures are presented. Upstream at x=8.4d, the increasing jet temperature leads to a higher mixing and diffusion. The near wall mass fraction at a distance of x=8.4d is increased from 0.25 (isothermal) to 0.30 (Δ T=50 K) and finally reaches 0.35 at Δ T=100 K while the mass fraction on center line (nozzle axis) stays nearly constant at all temperatures. Unique center line mass fractions are confirmed from measurements in the orthogonal $x-z$ center plane. At the most upstream distance the integral mass fraction of each profile differs which makes it difficult to compare measurements. Reasons could include secondary flow effects, different initial densities of the injected air and increasing densities while the hot jet mixes with cold air from the inlet. The influence of density changes on the accuracy of mass fraction measurements requires further investigations.

6. Summary and conclusions

A combined PLIF and PIV system was applied to simultaneously measure mass fraction and velocity in the mixing zone of a coaxial jet in a turbulent duct flow at atmospheric pressure. The uncertainty of time-averaged velocity, mass fraction, Reynolds stress and turbulent mass flux over the number of samples is assessed in the turbulent shear layer using an empirical bootstrapping approach. From 3000 samples the statistical error of time-averaged velocity and mass fraction is below 1% while the error of Reynolds shear stress and turbulent mass flux is between $5-6\%$. During pulsed jet injection a strong asymmetric growth of the shear layer vortices leads to a even more skewed mass fraction profile in comparison with steady injection. Phase averaging of single shot PLIF-PIV measurements allows to track the asymmetric shear layer vortex evolvement and flow breakdown during a pulsation cycle with a resolution of 10°. Injection with increased jet temperature of 345 K and 395 K seems to slightly support mixing and diffusion upstream from 8 nozzle diameters. Confirmation of hot jet results requires further analysis of the influence of gas density variations on the accuracy of mass fraction measurements using acetone PLIF.

REFERENCES

[1] Efron Bradley and Robert J Tibshirani. An introduction to the bootstrap. *Monographs on statistics and applied probability*, 57, 1993.

[2] R. A. Bryant, J. M. Donbar, and J. F. Driscoll. Acetone laser induced fluorescence for low pressure/low temperature flow visualization. *Experiments in Fluids*, 28(5):471–476, 2000.

[3] J. Heinze, U. Meier, T. Behrendt, C. Willert, K. Geigle, O. Lammel, and Lückerath. Plif thermometry based on measurements of absolute concentrations of the oh radical. *International journal of research in physical chemistry and chemical physics*, 225(11–12):1315–1341, December 2011.

[4] J. Klinner, V. Mayer, J. Heinze, and C. Willert. Simultaneous measurements of mixing fraction and velocities of a coaxial jet in a turbulent channel flow. In *17th Int Symp on Applications of Laser Techniques to Fluid Mechanics*, 2014.

[5] A. Lozano, B. Yip, and R.K. Hanson. Acetone: a tracer for concentration measurements in gaseous flows by planar laser-induced fluorescence. *Experiments in Fluids*, 13(6):369–376, 1992.

[6] Jason Stafford, Ed Walsh, and Vanessa Egan. A statistical analysis for time-averaged turbulent and fluctuating flow fields using particle image velocimetry. *Flow Measurement and Instrumentation*, 26(0):1 – 9, 2012.

[7] Mark C. Thurber, Frédéric Grisch, Brian J. Kirby, Martin Votsmeier, and Ronald K. Hanson. Measurements and modeling of acetone laser-induced fluorescence with implications for temperature-imaging diagnostics. *Appl. Opt.*, 37(21):4963–4978, Jul 1998.

[8] Heinrich Vollmers. Detection of vortices and quantitative evaluation of their main parameters from experimental velocity data. *Measurement Science and Technology*, 12(8):1199, 2001.

[9] ChristianE. Willert. High-speed particle image velocimetry for the efficient measurement of turbulence statistics. *Experiments in Fluids*, 56(1), 2015.

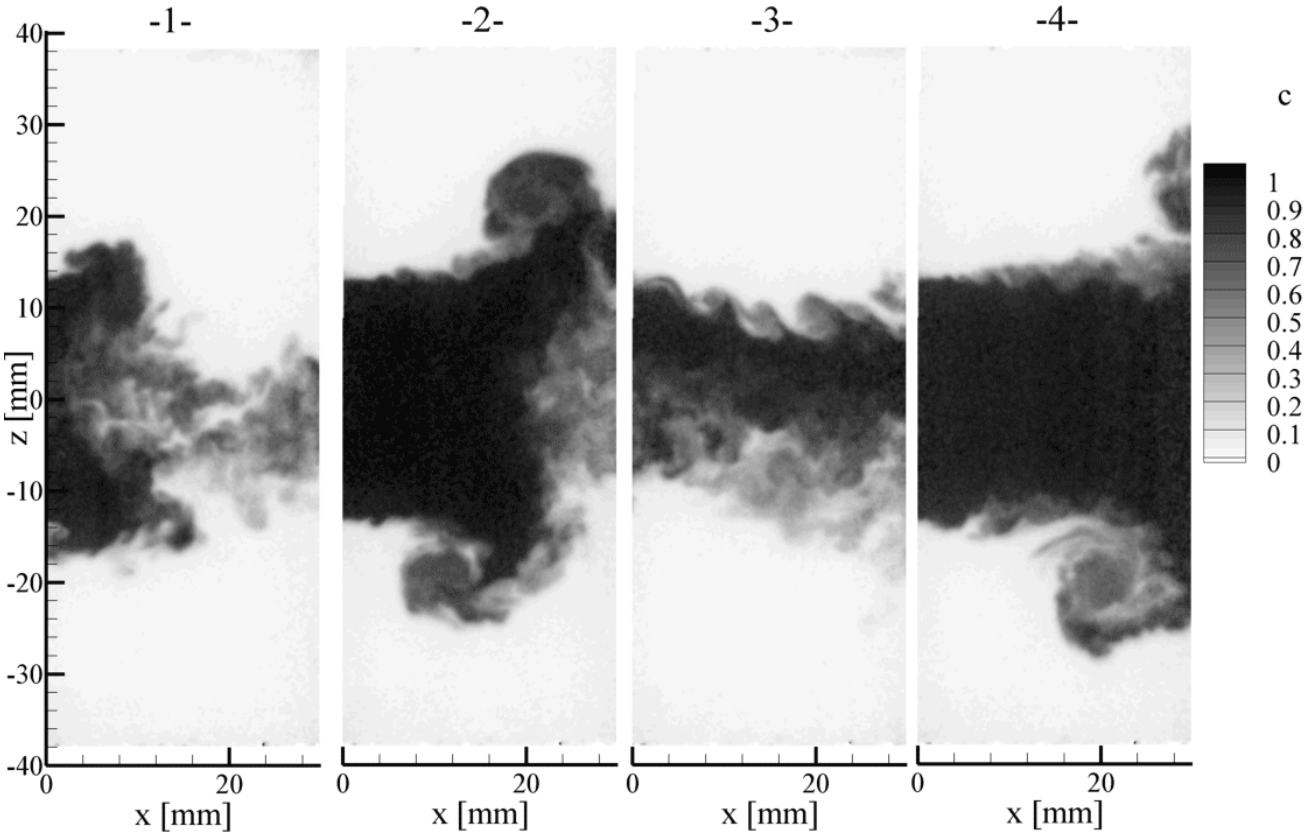

Figure 10: Snapshots of the concentration distribution in the $x-z$ center plane near the bend exit with pulsed injection

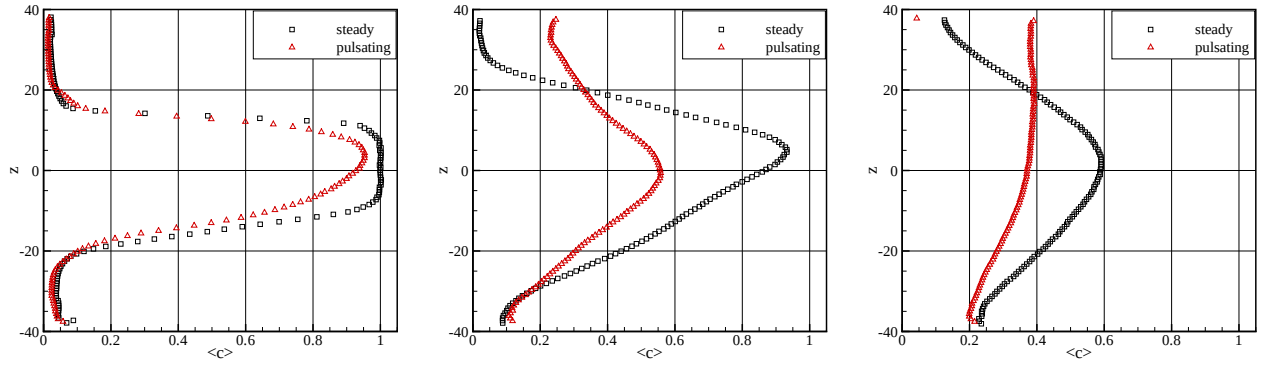

Figure 11: Isothermal mass fraction during pulsed and steady injection in the $x-z$ center plane: $x = 0.4d$ (left), $x = 3.2d$ (middle) and $x = 6d$ (right)

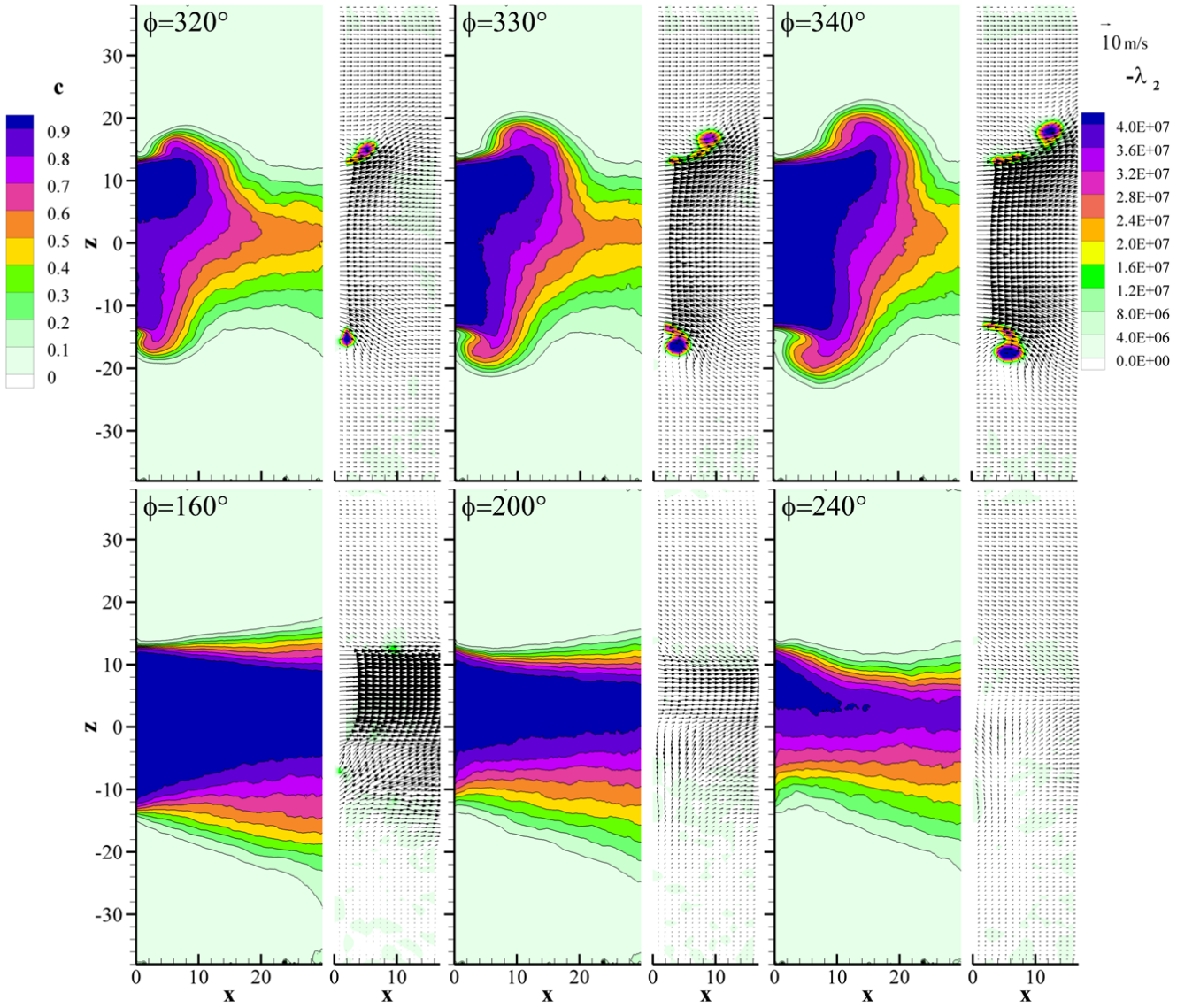

Figure 12: Phase averaged concentration and velocity fields in the $x-z$ center plane at the beginning of injection (top) and during flow breakdown (bottom)

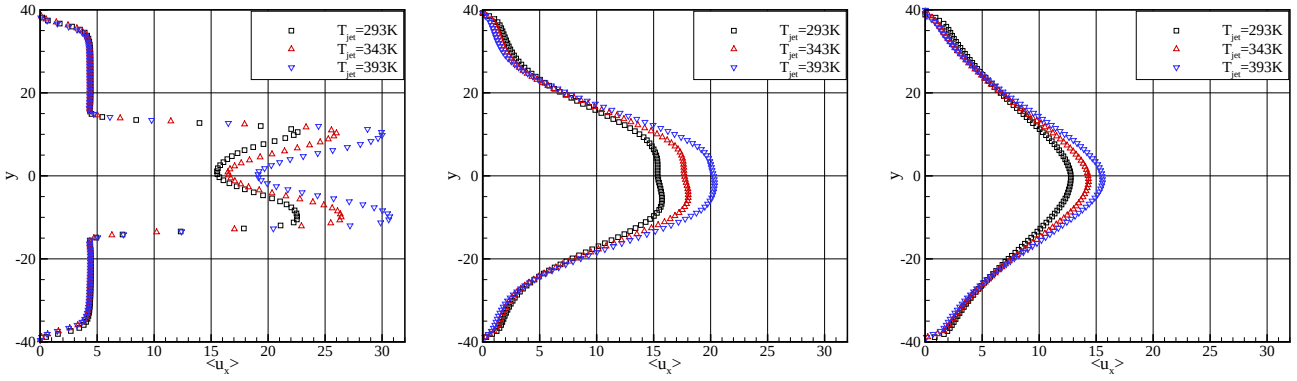

Figure 13: Axial velocity at increasing jet temperatures in the in the $x-y$ center plane: $x = 0.4d$ (left), $x = 4.4d$ (middle) and $x = 8.4d$ (right); $T_{inlet} = 293K$

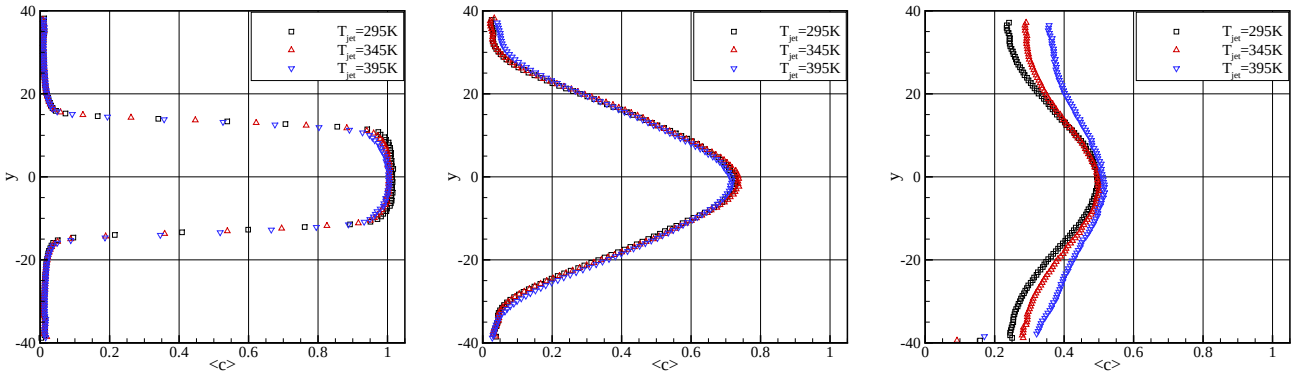

Figure 14: Mass fraction at increasing injection temperatures in the in the $x-y$ center plane: $x = 0.4d$ (left), $x = 4.4d$ (middle) and $x = 8.4d$ (right)